PNAS RESEARCH ARTICLE | CHEMISTRY

Atomic observation and structural evolution of covalent organic framework rotamers

Tengwu Zeng[a,1], Yang Ling[a,b,1], Wentao Jiang[a,1], Xuan Yao[a], Yu Tao[a], Shan Liu[a], Huiyu Liu[a], Tieying Yang[c], Wen Wen[c], Shan Jiang[a,b], Yingbo Zhao[a,b], Yanhang Ma[a,b], and Yue-Biao Zhang[a,b,d,2]

Edited by Omar Yaghi, University of California, Berkeley, CA; received November 21, 2023; accepted December 18, 2023

Dynamic 3D covalent organic frameworks (COFs) have shown concerted structural transformation and adaptive gas adsorption due to the conformational diversity of organic linkers. However, the isolation and observation of COF rotamers constitute undergoing challenges due to their comparable free energy and subtle rotational energy barrier. Here, we report the atomic-level observation and structural evolution of COF rotamers by cryo-3D electron diffraction and synchrotron powder X-ray diffraction. Specifically, we optimize the crystallinity and morphology of COF-320 to manifest its coherent dynamic responses upon adaptive inclusion of guest molecules. We observe a significant crystal expansion of 29 vol% upon hydration and a giant swelling with volume change up to 78 vol% upon solvation. We record the structural evolution from a non-porous contracted phase to two narrow-pore intermediate phases and the fully opened expanded phase using *n*-butane as a stabilizing probe at ambient conditions. We uncover the rotational freedom of biphenylene giving rise to significant conformational changes on the diimine motifs from *synclinal* to *syn-periplanar* and *anticlinal* rotamers. We illustrate the 10-fold increment of pore volumes and 100% enhancement of methane uptake capacity of COF-320 at 100 bar and 298 K. The present findings shed light on the design of smarter organic porous materials to maximize host–guest interaction and boost gas uptake capacity through progressive structural transformation.

reticular chemistry | covalent organic frameworks | dynamic response | gas storage | porous materials

Significance

Dynamic responses of covalent organic frameworks (COFs) are poorly understood at the atomic precision due to their conformation diversity and rapid interconversion. Here, we report the atomic observation and structural evolution of COF rotamers featuring with the diimine motifs switch from *synclinal* to *syn-periplanar* and *anticlinal* conformations. Such mechanism gives rise to a giant crystal expansion up to 78 vol% upon adaptive inclusion of guest molecules and a significant enlargement of pore volume by 10-fold. These results elaborate the delicate control of framework flexibility on organic porous materials for maximizing host–guest interaction and boosting their gas storage capacity through sequential framework transitions upon adaptive gas adsorption.

Dynamic 3D covalent organic frameworks (dynaCOFs) (1–5) are constructed by stitching organic building units through strong covalent bonds into interwoven networks to achieve exceptional chemical stability, concerted structural switchability, and guest-adaptive flexibility (6–8), featuring a new form of soft porous crystals (9–16). Hints of dynamic response to gas molecules have been reported via the stepwise and hysteresis adsorption in imine-linked 3D COFs (17–21). Yet, the atomic-level characterization of their dynamics remains largely unstudied (7, 22–25). We and others have developed the optimization preparation of COF samples (22–25) and the atomic-level characterization of dynamic structural transformation (18, 26–31) by advanced techniques, such as cryo-three-dimensional electron diffraction (3D ED), synchrotron ex situ powder X-ray diffraction (PXRD), and in situ PXRD during gas adsorption, for establishing the correlation between dynamic structures and their corresponding functional properties (32–38). We have uncovered the guest-dependent dynamics of COF-300-V prepared by a ventilation-vial synthetic protocol, featuring a significant crystal contraction upon hydration and a giant swelling of up to 50 vol% upon adaptive inclusion of organic vapors (22). A pedal motion of the diimine organic motif is suggested, considering the rotational freedom of the single bonds, allowing the framework to adapt itself to a wide variety of guest molecules and different loadings (19, 22). However, the isolation and observation of such COF rotamers remain challenging due to their comparable free energy and subtle rotational energy barrier. As the expanded isoreticular structure to COF-300, COF-320 is an ideal platform to delve deeper with a higher level of complexity due to additional rotational freedom of sigma bond between phenyls in extended ditopic linker. Controversially, "atropisomers" have been recently reported in COF-320 with multiple gas-triggered flexibilities at low temperatures, which suggested that interwoven frameworks prohibit the free rotation of imine linkages (39).

Herein, we report the atomic observation and structural evolution of COF rotamers (40)—a phenomenon that occurs due to the rotational freedom of the diimine organic building unit (Fig. 1) for boosting the overall gas uptake capacity. Specifically, our efforts have led to the enhanced crystallinity and morphology of COF-320 for manifesting its crystal dynamics as shown by the step-wise gas adsorption isotherms of methane (CH_4, 112 K) and *n*-butane (C_4H_{10}, 298 K), as well as the significant changes in PXRD patterns for the activated, solvated, and hydrated samples. A significant crystal expansion of 29

Author contributions: Y.-B.Z. designed research; T.Z., Y.L., W.J., X.Y., Y.T., and S.L. performed research; T.Y. and W.W. contributed new reagents/analytic tools; T.Z., Y.L., W.J., H.L., S.J., Y.Z., Y.M., and Y.-B.Z. analyzed data; and T.Z. and Y.-B.Z. wrote the paper.

The authors declare no competing interest.

This article is a PNAS Direct Submission.

[1]T.Z., Y.L., and W.J. contributed equally to this work.

[2]To whom correspondence may be addressed. Email: zhangyb@shanghaitech.edu.cn.

This article contains supporting information online at https://www.pnas.org/lookup/suppl/doi:10.1073/pnas.2320237121/-/DCSupplemental.

Published January 22, 2024.

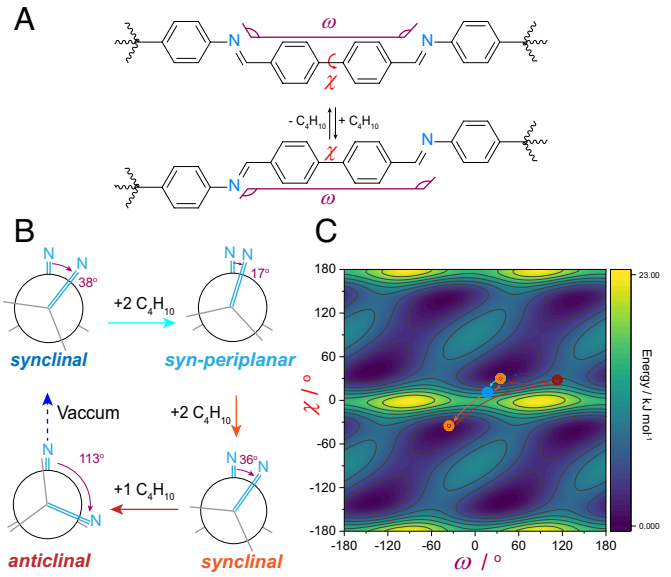

Fig. 1. Conformational parameters of COF rotamers (*A*), the Newman projections (*B*), and the rotational energy landscape of rotamers observed in COF-320-V (*C*).

vol% upon hydration and a giant large framework swelling up to 78 vol% upon solvation, as compared to the activated phase, were determined by 3D ED and synchrotron PXRD. Through in situ PXRD during C_4H_{10} uptake at 298 K, we unveil the rotamers of COF-320 that feature various torsion angles of the diimine linkers (ω, Fig. 1 *A* and *B*) switching from *synclinal* (ω = 38°) to *syn-periplanar* (ω = 17°), *synclinal* (ω = 35°/324°), and *anticlinal* (ω = 113°) conformations during the C_4H_{10} adsorption process (Fig. 1*B*). Such rotational freedom is correlated to the torsion angle of 4,4′-the biphenyl motif (χ) mapped in the energy landscape (Fig. 1*C*) since imine bonds tended to be coplanar with adjacent phenyl rings for conjugation resonance. Ultimately, such a concerted structural transition from non-porous to highly porous dramatically affected high-pressure methane uptake, boosting its uptake capacity by 100%. These results shed light on exploring COF rotamers by harnessing the crystallinity, dynamics, and porosity of organic porous materials for maximizing host–guest interactions and boosting gas uptake capacity.

Results and Discussion

Facile Preparation of COF-320 via the Ventilation-Vial Synthetic Protocol. COF-320 is constructed from the imine-condensation of TAM [Tetra-(4-anilyl)-methane] and BPDA (4,4′-biphenyldialdehyde) (Fig. 2*A*), which was prepared through the conventional sealed-tube protocol at a relatively higher temperature (18), resulting in aggregated crystallites (denoted as COF-320-T). Through a one-step nucleation/crystal growth mechanism, we previously reported a ventilation-vial synthetic protocol for the facile preparation of COF-300 at milder conditions (22). Herein, we employed this protocol for optimizing the preparation of COF-320 samples (denoted as COF-320-V) by varying the amount of modulator (aniline), catalyst (acetic acid), reaction solvents (1,4-dioxane and pyridine), and reaction temperatures (60 to 120 °C) and examined their resulting crystal morphologies and PXRD patterns (*SI Appendix*, Table S1). By adding aniline as a modulator, the reaction undergoes an imine-exchange mechanism that slows down the imine formation to produce well-defined crystal morphology with narrow distribution (7, 32–33), whereas more amount of aniline resulted in the slender crystals. Decreasing the pyridine ratio generally led to crystal aggregations while increasing the reaction temperatures afforded narrow-down crystal sizes. We attribute the addition of pyridine to improving the solubility of intermediate oligomers and preventing the deactivation of the amines with regulated reaction kinetics. Scanning electron microscope (SEM) imaging of COF-320-T (Fig. 2*B*) exhibited sub-micron-sized aggregated crystallites. The COF-320-V (Fig. 2*C*) shows micron-sized crystals in well-defined prismatic shapes with the crystal size distribution centered at 1.1 μm (*SI Appendix*, Fig. S1).

After washing and activation, thermal gravimetric analyses (TGA, *SI Appendix*, Fig. S2) confirm the complete removal of guest molecules and reveal high thermal stabilities of up to 450 °C for COF-320-V, outperforming that of -T. Fourier Transform Infrared (FT-IR) spectroscopy (Fig. 2*D*) validates the formation of imine bonds with the characteristic –C=N– stretching at 1,624 cm^{-1} being observed along with the elimination of starting materials as evidenced by the complete absence of –C=O stretching at 1,683 cm^{-1} for COF-320-V compared to -T. Solid-state CP/MAS ^{13}C NMR spectroscopy (Fig. 2*E*) proved the full conversion of imine linkages by the absence of aldehyde ^{13}C signals for both the activated COF-320-V and -T. However, significant differences in the ordering of local chemical environments were seen from the sharp chemical shifts for COF-320-V with a full width at half maximum (FWHM) as narrow as 65 Hz compared to COF-320-T having an FWHM of 100 Hz at 160 ppm. The chemical shifts of solvated and hydrated COF-320-V were even sharper with the FWHM of 42.8 and 17.9 Hz at 65 ppm, respectively (*SI Appendix*, Fig. S3). Chemical shift assignments were aided through CPPI (cross-polarizationpolarization inversion)-MAS experiments with varied polarization inversion times (*SI Appendix*, Figs. S4 and S5).

Comparison of the PXRD patterns of COF-320-V with the starting materials (*SI Appendix*, Fig. S6) excludes the possibility of recrystallization of reactants. Enhancement of crystallinity is evidenced by the sharper PXRD patterns of COF-320-V (Fig. 2*F*) with the FWHM of the peaks at 2θ ~ 8.6° as narrow as 0.217° compared to -T (FWHM ~0.351°). This is consistent with the PXRD comparison of solvated (COF-320-Vs) and hydrated (COF-320-Vh) phases (*SI Appendix*, Fig. S7 and Table S2).

Manifestation of Dynamic Response during Gas Adsorption. Gas adsorption isotherms of various molecules manifest the dynamic responses for COF-320-V compared to -T (*SI Appendix*, section B). Notably, the stepwise CH_4 adsorption isotherm at 112 K of COF-320-V (Fig. 2*G*) exhibits stoichiometric uptakes with the first plateau of 2 mol mol^{-1} at P/P_0 ~ 0.02, the second plateau of 9 mol mol^{-1} at P/P_0 ~ 0.1 with the third plateau of 12 mol mol^{-1} at P/P_0 ~ 0.22, and then saturation with 16 mol mol^{-1} uptake at P/P_0 ~ 0.4, respectively. In contrast, COF-320-T displayed a quasi-knee-shaped isotherm with inconspicuous desorption hysteresis. Nevertheless, the saturated CH_4 uptakes for both samples suggest the same pore volumes of 0.89 cm^3 g^{-1}, indicating the same connectivity and degree of interpenetration but varying dynamic responses.

The C_4H_{10} adsorption isotherm at 298 K of COF-320-V (Fig. 2*H*) exhibited a stepwise adsorption behavior and hysteresis desorption with three plateaus. Upon stoichiometric inclusion of C_4H_{10} molecules, the pore volume reaches 0.28 cm^3 g^{-1} with 2 mol mol^{-1} uptake at 15 kPa, 0.57 cm^3 g^{-1} with 4 mol mol^{-1} uptake at 40 kPa, and 0.72 cm^3 g^{-1} with 5 mol mol^{-1} uptake at 100 kPa. In comparison, the C_4H_{10} uptake of COF-320-T displays a fluctuating sigmoidal shape to reach a similar saturated uptake, indicating the lack of coherency for structural transformation. The trend is observed in the vapor adsorption isotherms (THF at 283 K and 1,4-dioxane at 298 K, *SI Appendix*, Figs. S9 and S10) with similar calculated pore volumes at each stage (*SI Appendix*, Table S3). These consistent three-step

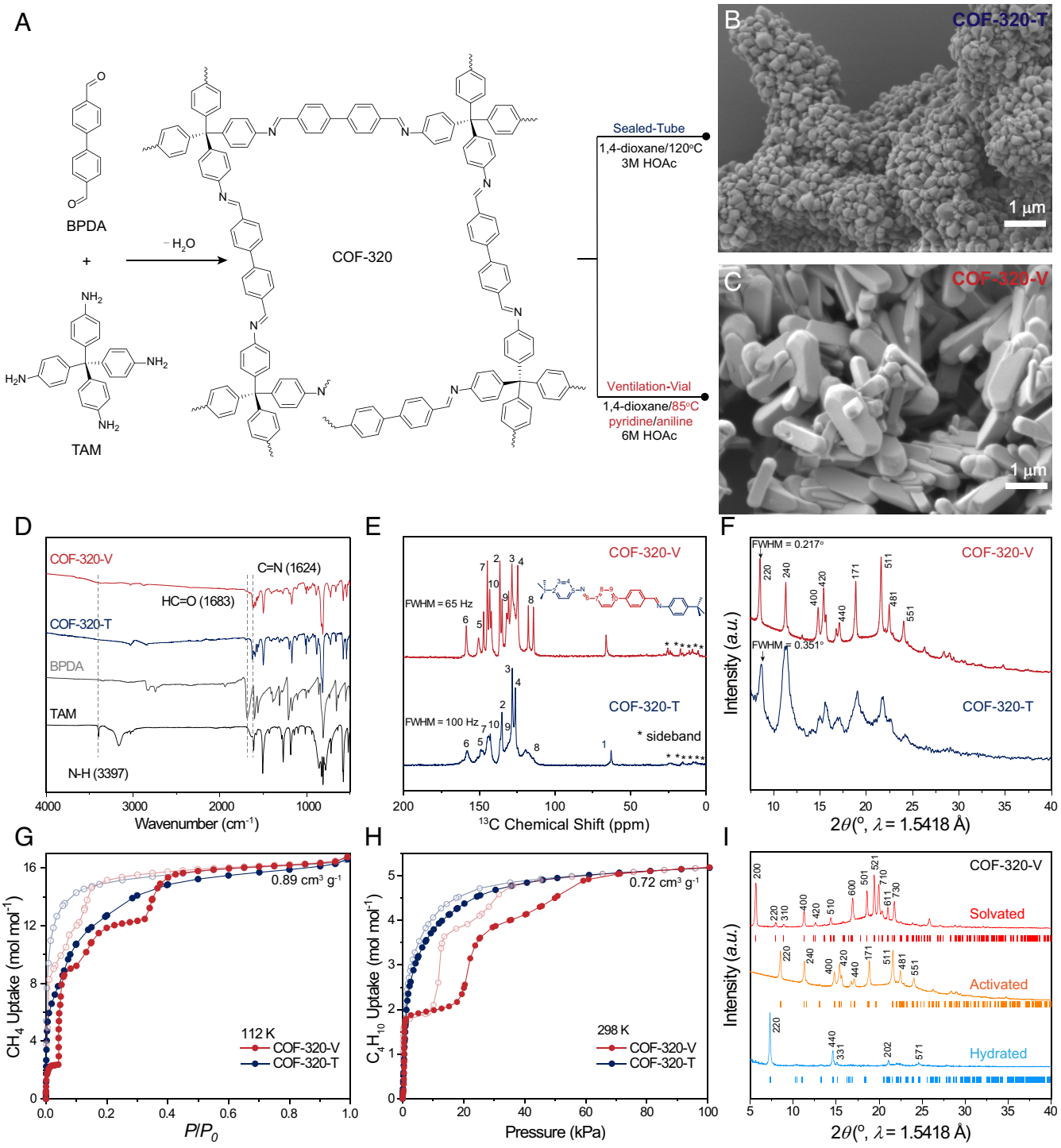

Fig. 2. Optimal preparation of COF-320 with enhanced crystallinity and uniform morphology for manifesting dynamics. (*A*) Conventional sealed-tube (-T) and the ventilation-vial (-V) synthetic protocols and their resulting morphologies for COF-320-T (*B*) and -V (*C*), respectively. (*D*) Comparison of IR spectra of the COF-320-V with -T and their starting materials. (*E*) Comparison of solid-state CP/MAS ^{13}C NMR spectra of COF-320-V and -T (asterisks, spinning sidebands). (*F*) Comparison of PXRD patterns and FWHM of COF-320-V and -T. Gas adsorption isotherms of CH_4 at 112 K (*G*) and C_4H_{10} at 298 K (*H*) for COF-320-V and -T. (*I*) Comparison of PXRD patterns of the activated, hydrated, and solvated samples of COF-320-V.

adsorption behaviors suggest the existence of metastable intermediate states stabilized by gas molecules during adsorption (1).

Structural transformations of COF-320-V during adsorption of 1,4-dioxane and H_2O vapors were evidenced by comparing PXRD patterns of the solvated, activated, and hydrated samples (Fig. 2*I*). In contrast with the hydration-induced crystal contraction in COF-300 (22), the left-shifted PXRD patterns indicate a crystal expansion upon hydration.

Atomic-Level Characterization of Guest-Dependent Dynamics of COF-320. The single-crystal structures of COF-320-V (Fig. 3*A* and *SI Appendix*, section C) were elucidated through cryo-3D ED (26, 32–33). The significantly improved crystallinity of COF-320-V yielded high-resolution ED data for the solvated, activated, and hydrated phases, enabling precise ab initio structure determination through direct methods (*SI Appendix*, Table S4). COF-320-Vh crystallized in the orthogonal space group of *Fdd*2

(*No*. 43) with lattice constants of a = 34.43 Å, b = 34.09 Å, c = 8.69 Å, and V = 10,454 Å^3 (*SI Appendix*, Figs. S12, S15, and S18). Upon removal of water molecules, the unit cell parameters for the activated phase were determined as follows: a = 23.93 Å, b = 41.94 Å, c = 8.09 Å, and V = 8,124 Å^3 with the same space groups *Fdd*2 (*No*. 43, *SI Appendix*, Figs. S11, S14, and S17). In the case of the solvated COF-320-V, the crystal crystallizes in the tetragonal space group of *I*-42*d* (*No*. 122), with larger unit cell parameters of a = 31.12 Å, c = 7.67 Å, and V = 7392 Å^3 with ED data resolution up to 0.8 Å and completeness of 97% (*SI Appendix*, Figs. S13, S16, and S19).

The crystal structures and structural transformation of the bulk samples were further determined through ex situ synchrotron PXRD with Rietveld refinements for the solvated, activated, and hydrated phases (Fig. 3*B* and *SI Appendix*, Fig. S20 and section D). Notably, COF-320-V exhibited significant crystal expansion of ~29 vol% upon hydration for one chemical formula unit ($C_{53}H_{36}N_4$), with the channels adapting accordingly to the inclusion of H_2O

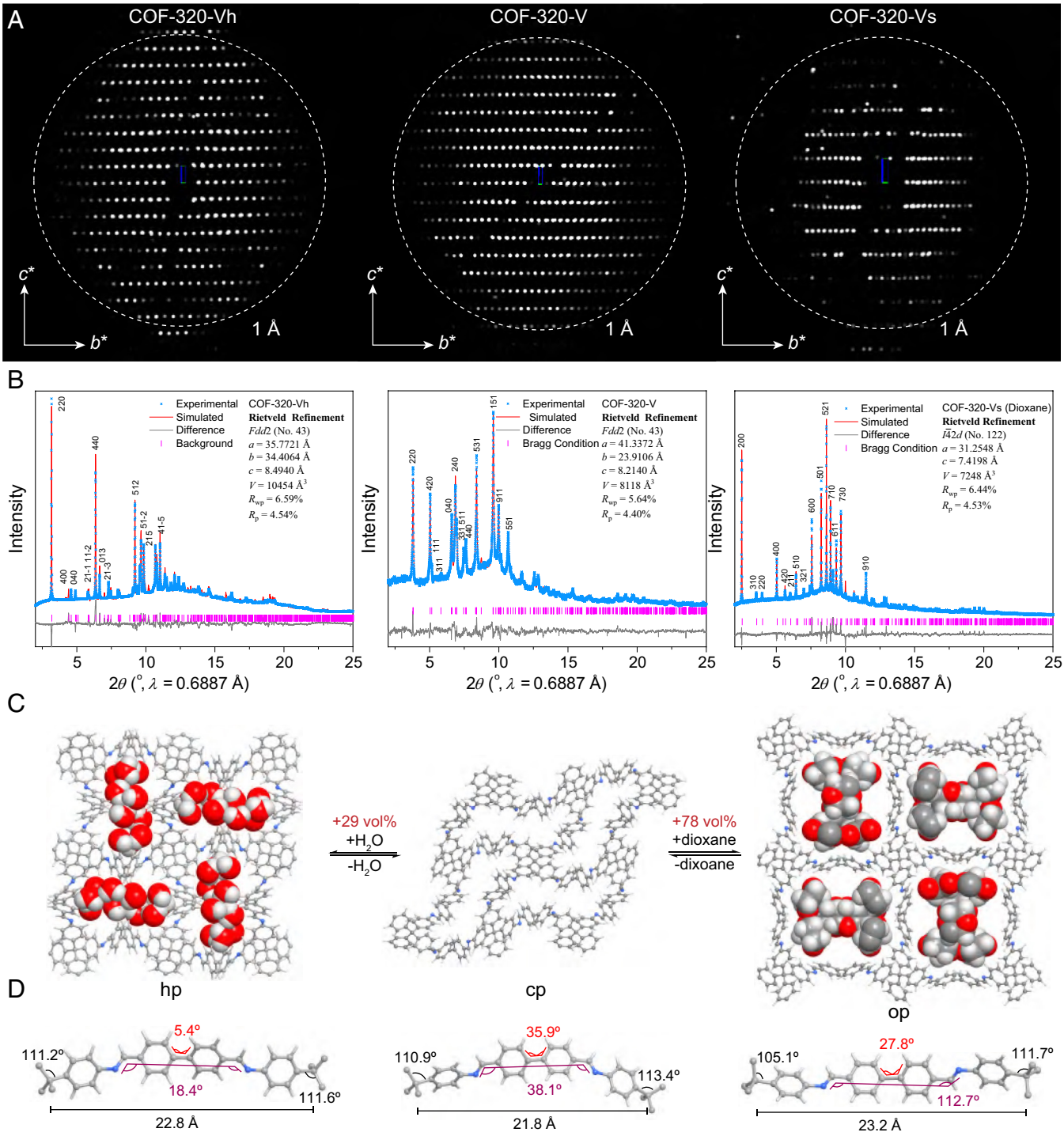

Fig. 3. Atomic-level characterization of COF rotamers featuring rotational freedom of the diimine organic motif and significant crystal expansion from activated (COF-320-V) to hydrated (COF-320-Vh) and solvated (COF-320-Vs) phases. (*A*) 3D ED data with a resolution better than 1.0 Å projected along the [100]. (*B*) Indexing and Rietveld refinement of synchrotron PXRD patterns (blue) against the crystal structures determined by cryo-3D ED. (*C*) Atomic-level pore changes by combining ab initio structure solutions from 3D ED data and Rietveld refinements of synchrotron PXRD patterns. (*D*) Geometric and conformational changes of the COF rotamers featuring the rotational freedom of the 4,4′-biphenylene and the diimine motifs.

(Fig. 3*C*). Remarkably, a large amplitude of crystal expansion up to ~78 vol% is also observed in COF-320-V upon adaptive inclusion of 1,4-dioxane (*SI Appendix*, Fig. S21 and Table S6). The closed pores of COF-320-V (cp, *Middle* in Fig. 3*C*) significantly expanded into rectangular-shaped channels (op), as featured by a 10-fold increment in pore volumes from 0.08 to 0.84 cm^3/g (estimated using PLATON) (41).

The adaptivity of COF-320-V to various guest molecules mainly comes from the conformational diversity of the diamine organic linkers (Fig. 3*D*). The distance between two connected tetrahedral nodes of COF-320-V expands from 21.8 to 23.2 and 22.8 Å upon solvation and hydration, respectively. The –N=C–biphenyl–C=N– torsion angle (ω) of COF-320-V rotates from 38° to 112° and 18° owing to the rotation freedom of the 4,4′-biphenyl motifs.

Dynamic Structural Evolution during Adsorption. Considering the stepwise uptakes and facile handling of C_4H_{10}, we focused on trapping the intermediate phases during gas uptake using both in situ and ex situ PXRD patterns. For further elucidating how the framework adapts to the guest molecules to perform the dynamic structural transformation, the isotherm of C_4H_{10} (Fig. 4*A*) and in situ PXRD patterns of COF-320-V are collected under representative C_4H_{10} concentrations (Fig. 4*B*).

As depicted in Fig. 4*A*, C_4H_{10} isotherm at 298 K showed stepwise uptake and hysteresis desorption with three plateaus featuring stoichiometric adaptive inclusion. With 2 mol mol^{-1} uptake at 15 kPa, the pore volume reaches 0.28 $cm^3\ g^{-1}$; with 4 mol mol^{-1} uptake at 40 kPa, the pore volume reaches 0.57 $cm^3\ g^{-1}$ with 5 mol mol^{-1} uptake at 100 kPa, the pore volume reaches 0.72 cm3 g^{-1}. As shown in the contour plot (Fig. 4*B*), PXRD patterns of COF-320-V remained constant under 0.04 kPa of C_4H_{10}, which switched to an intermediate phase (denoted as COF-320-V-ip1), with concentration increased slightly from 0.04 kPa to 1 kPa. The transition to the second intermediate phase (COF-320-V-ip2) was completed under 40% concentration, which correlated to 4 mol mol^{-1} C_4H_{10} uptake in the adsorption isotherm (Fig. 4*A*). The complete expansion upon 80 kPa was suggested by vanishing a peak in $2\theta = 6.74°$. Interestingly, during desorption, the framework shrinks into two intermediate phases at lower concentrations than the adsorption branch (*SI Appendix*, Figs. S23 and S24) due to the dynamic nature of the diimine linkages.

Structural transformations were revealed clearly by ex situ synchrotron PXRD analyses of two metastable intermediate structures (Fig. 4 *C* and *D* and *SI Appendix*, section E). The specific C_4H_{10} concentrations were determined by in situ PXRD analyses and were dosed into a glass tube holding the activated sample. The GCMC (GrandCanonical Monte Carlo)-simulated C_4H_{10} adsorption isotherms at 298 K for the four obtained structures are consistent with the three plateaus of the experimental one, further demonstrating the structure transformation during the adsorption process (Fig. 4*A*). Activated COF-320-V (cp) represents a synclinal conformation of the diimine linker with $\omega = 38°$, resulting in a non-porous state.

Through DFT calculation, we obtained the precise position of adsorptive sites for C_4H_{10} molecules in channels and their self-adaptive arrangements corresponding to the structure transformation in COF-320-V-ip1, -ip2, and -op (Fig. 4*C*), which also match the GCMC-simulated density profiles (*SI Appendix*, Fig. S29). Upon adaptive inclusion of 2 mol mol^{-1} of C_4H_{10}, COF-320-V-ip1 exhibits a syn-periplanar conformation of the diimine linker with $\omega = 17°$, leading to the crystal expansion of 25 vol% without changing the crystallography symmetry (space group: *Fdd2*, *No*. 43, *SI Appendix*, Fig. S26). To deepen our understanding of the host–guest interaction, we employed the Independent Gradient Model based on Hirshfeld partition of molecular density (IGMH) (42, 43) method to visualize the intermolecular interactions. The C_4H_{10} molecules at the narrow channel were divided by twisted 4,4′-biphenyl motifs to stabilize through interaction with the pore wall, mainly through the -CH···HC- van der Waals interaction (*SI Appendix*, Fig. S28).

Further incorporation of 2 mol mol^{-1} of C_4H_{10}, COF-320-V-ip2 represents the synclinal and anti-periplanar conformation of the diamine linker with $\omega = 35°$ and $\omega = 324°$ for two asymmetric units due to the lower crystal symmetry (space group: $I2_12_12_1$, *No*. 24, *SI Appendix*, Fig. S27), enabling a crystal expansion of 27 vol% and enlargement of channels into a rectangle shape. The C_4H_{10} molecules are re-arranged into different clusters within adjacent channels, docking at the corner of the channel through van der Waals interactions between N and H with the linkers and the C–H with phenyl rings interaction with the two benzene rings of the TAM molecule (*SI Appendix*, Fig. S28). The complete open phase (op) adopted anticlinal conformation with $\omega = 113°$, suggesting less expansion after the adaptive inclusion of *n*-butane flow than observed in 1,4-dioxane solvent (*SI Appendix*, Fig. S25). Five C_4H_{10} molecules are located at the channel of the op, with four of them possessing C–H···π interaction with the host framework and one of them confined by the host–guest interactions.

Boosting Methane Uptake Capacity. Although COFs are robust, light, and metal-free porous materials with potential cost plunges upon scale-up production, their gas storage applications are underdeveloped, which might be attributed to the weak interaction with non-polar and pure organic surfaces (44–46). The adaptive inclusion of gas within dynaCOFs enables the synergistic interplay of multiple weak interactions and shape recognition for maximal host–guest interaction and rearrangement of guest molecules to maximize the adsorption capacity. The high-pressure (0 to 100 bar) total CH_4 uptakes at 298 K of COF-320-V (Fig. 5*A*) exhibited stepwise adsorption and hysteresis desorption isotherms. The total uptake at 100 bar and 298 K is correlated to a fully open state since we have measured the higher pressure (0 to 200 bar) CH_4 uptakes at 283, 298, and 308 K (*SI Appendix*, Figs. S30 and S31). The stepwise uptake is reproducible for three cycling tests due to the great resilience endowed by the covalent linkages (*SI Appendix*, Fig. S32). In contrast, the previously reported CH_4 uptake (18) only shows one-step uptake and lower capacity. With the dynamic response to CH_4 gas, the COF-320-V represents boosted methane uptake at 298 K of 66% increment at 80 bar and 100% enhancement at 100 bar reaching 315 $cm^3_{STP}\ g^{-1}$ and 224 mg g^{-1} comparable to COF-103 (229 mg g^{-1}) (46). Nevertheless, such dynaCOFs could have advantages in onboard methane storage to improve their packing density with the contracted phase (cp) and to function with the expanded phase for maximal gas uptake, optimal working capacity, and intrinsic thermal management (47).

Since the CH_4 (112 K) adsorption isotherm of COF-320-V also represents stepwise uptakes (Fig. 2*G*), we conducted the GCMC simulation of the CH_4 adsorption isotherms at 112 K (*SI Appendix*, Figs. S33 and S34) for the cp, ip1, ip2, and op structures refined from ex situ PXRD analyses during C_4H_{10} adsorption, which match well with its three uptake plateaus. These results indicate that COF-320-V undergoes a similar structural transformation during CH_4 adsorption. We then simulated the CH4 absolute uptakes at 298 K and 0 to 100 bar for op phases (Fig. 5*B*), suggesting that the structure was fully opened upon 100 bar. Compared with the simulated CH_4 uptake of the op structure, the experimental CH_4 uptake with the dynamic structural transformation has reduced the gas uptake below 5.8 bar, showing the possibility of optimizing deliverable methane capacity by tuning flexibility. The probability of CH_4 adsorbates within the channels

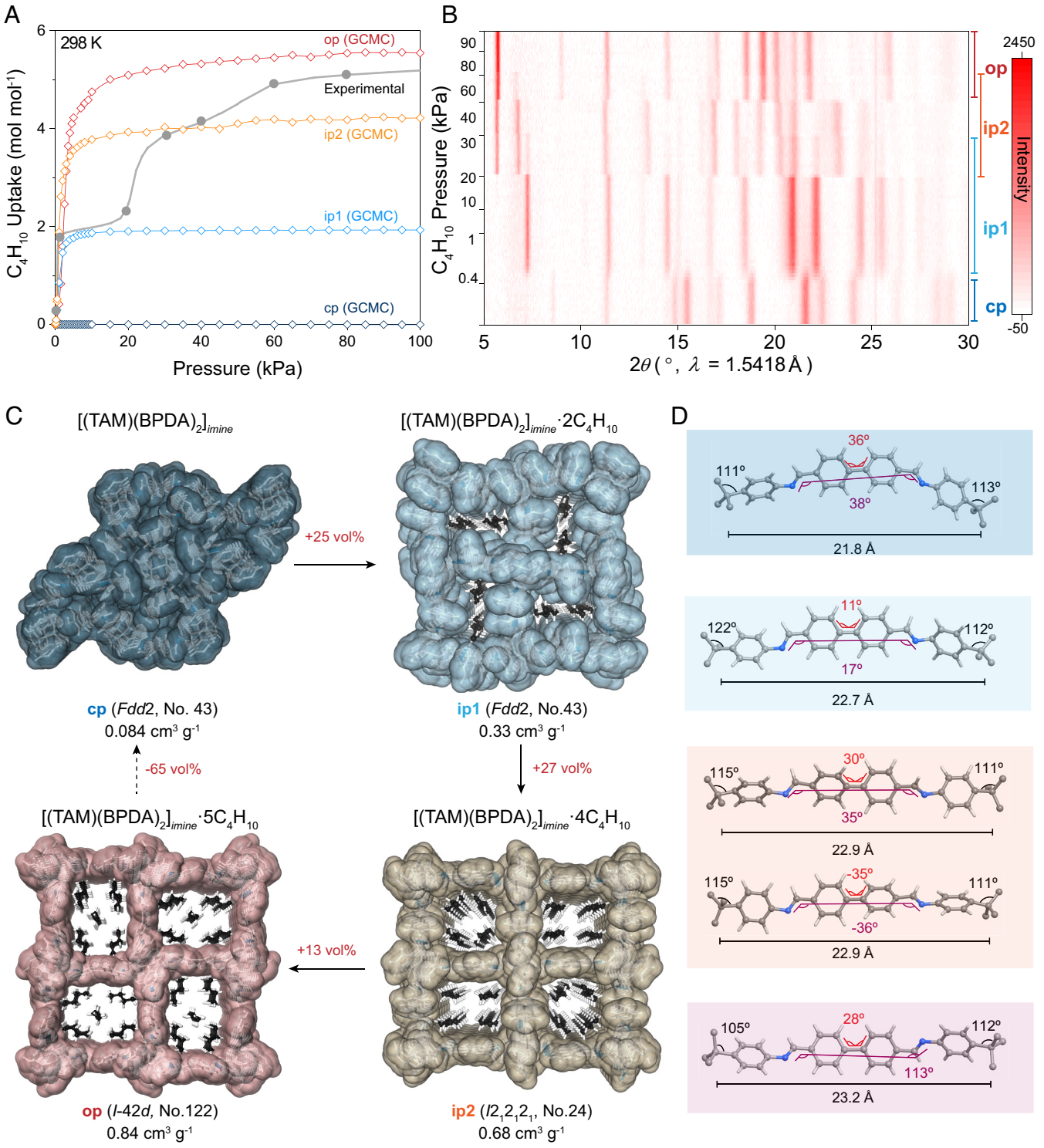

Fig. 4. Crystal structure evolution of COF rotamers during C_4H_{10} adsorption undergoing a cp, intermediate phases (ip1 and ip2), and an op of COF-320-V. (*A*) Theoretical adsorption isotherms of C_4H_{10} at 298 K through GCMC simulation of cp (navy), ip1 (blue), ip2 (orange), and op (red) compared with the experimental adsorption isotherm (gray). (*B*) Contour plot of in situ PXRD patterns of COF-320-V during dynamic C_4H_{10} adsorption under various concentrations of n-butane gas in N_2 carrier gas at ambient conditions. (*C*) Crystal structures of the cp, ip1, ip2, and op of COF-320-V determined by Rietveld refinements of synchrotron ex situ PXRD patterns and DFT calculation of gas adsorptive sites. (*D*) Geometric and conformational changes of the diimine organic linkers adapted to different loading of C_4H_{10} adsorbates.

(Fig. 5*C*) unveils the adapt inclusion of CH_4 gas molecules with maximal host–guest interaction at each state and the evolution of gas adsorptive sites for boosting gas storage capacity.

In summary, we have optimized the crystallinity and morphology of COF-320 through the ventilation-vial synthetic protocol to manifest structural dynamics during gas adsorption. Atomic-resolution determination of guest-dependent dynamics has shown a significant crystal expansion of 29 vol% upon hydration and a giant framework swelling up to 78 vol% upon adaptive inclusion of organic vapors in COF-320-V. The structural evolution of COF rotamers has shown a rotational freedom of the diimine linker motif switching from *synclinal* to *syn-periplanar*, *synclinal*, and *anticlinal*

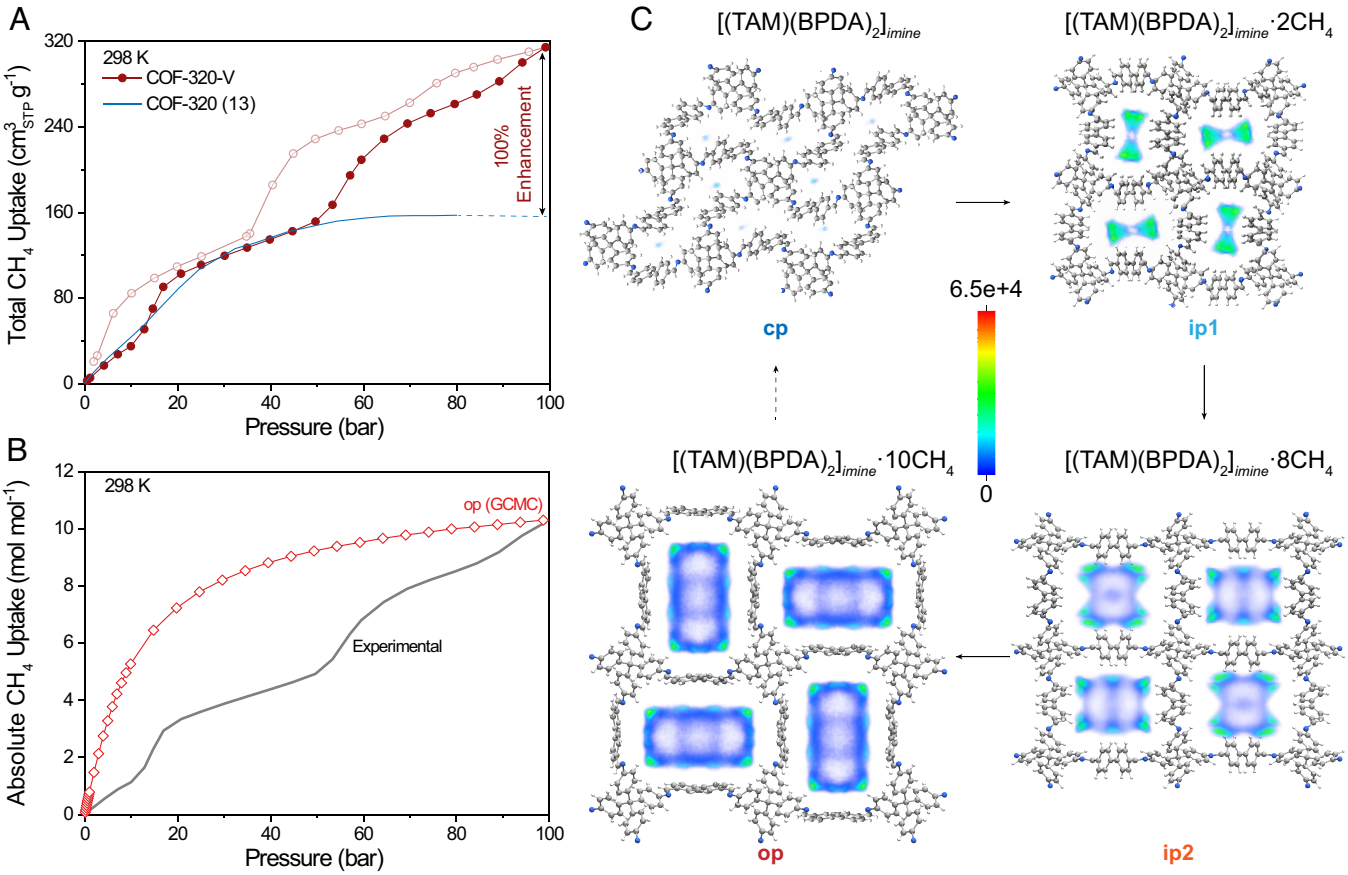

Fig. 5. Evaluation of methane uptake capacity of COF-320-V with the evolution of COF rotamers. (*A*) High-pressure (0 to 100 bar) CH_4 total uptake at 298 K of COF-320-V compared to the reported isotherm (13) of COF-320. (*B*) GCMC simulated high-pressure (0 to 100 bar) CH_4 absolute uptakes at 298 K of the op (red) of COF-320-V compared to the experimental (gray) CH_4 absolute uptake. (*C*) The probability of CH_4 adsorbed within the channels of cp, ip1, ip2, and op of COF-320-V through GCMC simulation.

conformations. The multistep adaptive inclusion adsorption of non-polar gas molecules enables the maximization of host–guest with only weak van der Waals interaction to interplay with the precision of host–guest recognition and adaption for higher gas uptake capacity without strong binding sites usually requiring metal centers. The conceptual advance of COF rotamers paves the way for achieving high uptake capacity and deliverable capacity by deliberate control of the dynamic responses of COFs for onboard methane storage, water harvesting, and other functional applications.

Materials and Methods

Materials and Instrumentation. BPDA (purity > 98%) was purchased from Adamas Co. TAM (purity > 97%) was purchased from Tensus Biotech Co. Aniline (AR, ≥99.5%), anhydrous 1,4-dioxane (AR, ≥99.5%), and anhydrous pyridine (AR, ≥99.5%) were purchased from J & K Scientific Co. Glacial acetic acid (AR, ≥99.5%) was purchased from Sinopharm Chemical Reagent Co.

FT-IR spectra were collected on a PerkinElmer ALPHA's Platinum ATR FT-IR spectrometer equipped with a single reflection diamond ATR module. Solid-state ^{13}C NMR (ssNMR) spectra were acquired on Bruker AVANCE III spectrometry (400 MHz). PXRD patterns were collected on a Bruker D8 advance diffractometer using Cu Kα radiation (λ = 1.5418 Å). The morphology of the microcrystals was examined on a JEOL JSM 7800F Prime SEM. Thermogravimetric analyses (TGA) were conducted on a PerkinElmer TGA 4000 TGA instrument with a heating rate of 5 °C min^{-1} under N_2 flow. Gas adsorption isotherms of N_2 (77 K) were collected from a Quantachrome Autosorb iQ_2 microporosity and specific surface area analyzer using liquid N_2 Dewar for temperature control. Vapor adsorption isotherms of tetrahydrofuran (283 K), 1,4-dioxane (298 K), and H_2O (298 K) were measured on a BELSORP MAX II or Aqua3 precious vapor adsorption analyzers. Dynamic vapor sorption (DVS) isotherms and cycling water uptakes were collected on a Surface Measurement Systems Resolution gravimetric DVS instrument.

Preparation of COF-320-V, $[(TAM)(BPDA)_2]_{imine}$. The mixture of TAM (23 mg, 0.05 mmol), BPDA (21 mg, 0.1 mmol), anhydrous 1,4-dioxane (0.25 mL), and pyridine (0.15 mL) is dispersed in a 5-mL ventilation vial with sonication, followed by the addition of aniline (0.06 mL) and acetic acid (6 mol L^{-1}, 0.2 mL). By heating the vial at 85 °C for 3 d, yellow microcrystals at the bottom were then isolated by centrifugation and washed with 1,4-dioxane exhaustively using a Soxhlet extractor for 1 wk. The resultant sample is activated by heating to 120 °C overnight under a vacuum of up to 10 mTorr to yield the activated sample of COF-320-V.

ssNMR Spectroscopy. ssNMR spectroscopy is performed with magic angle spinning (MAS) techniques on a Bruker AVANCE III HD 400 MHz wide-bore solid-state NMR spectrometer at a magnetic field of 9.4 T equipped with a standard Bruker MAS probe with 3.2 mm (o.d.) zirconia rotor. ^{13}C MAS NMR data were acquired at the Larmor frequency of 100.6 MHz. All the ^{13}C chemical shifts are referenced to tetramethyl silane at 0 ppm and calibrated using the carboxylic carbon of the glycine assigned to 176.2 ppm as a secondary reference. All the ^{13}C NMR spectra were carried out on a standard 3.2 mm double-resonance probe with a sample spinning rate of 12 kHz. ^{13}C cross-polarization (CP)-MAS experiments were carried out with a 1H $\pi/2$ pulse length of 3.5 μs, a contact time of 2 ms, a pulse delay of 5 s, and a SPINAL-64 at decoupling frequency of 81 kHz. The CPPI-MAS experiments were conducted to distinguish ^{13}CH, $^{13}CH_2$, $^{13}CH_3$, and quaternary carbons in the ^{13}C MAS NMR spectra with additional polarization inversion times.

3D-ED Structural Determination. 3D ED data were collected on the TEM JEM-F200 (JEOL Ltd., Schottky Electron Gun, 200 kV) equipped with a hybrid-pixel electron detector (Cheetah 1800, 512 × 512 pixels, pixel size 55 μm, Amsterdam Scientific Instruments) and the modified Instamatic software (48). The dose rate is about 0.38 e^{-1} $Å^{-2}$ s^{-1}. All the 3D ED data are processed and merged by the software XDS (49) and visualized by the software EDT-Process. Ab initio structure solutions were obtained using the intrinsic phasing method implemented in the SHELXT program (50). The structure refinements were performed via the SHELXL program (51) in Olex2 packages (52). Anisotropic refinements were used for all non-hydrogen atoms.

The specimen of COF-320-V-activated was prepared by dusting the COF-320-V powder onto a copper grid with ultrathin carbon membrane, which is further transferred to TEM (293 K, $< 8 \times 10^{-6}$ Pa) with a high-tilting holder. The COF-320-V-solvated specimen was prepared by dispersing the COF-320-V in 1,4-dioxane and dropping casting onto a glass slide. Upon drying the surrounding solvent, the sample was pressed onto the copper grid with ultrathin carbon membrane by two glass slides, which was transferred to TEM with a high-tilting cryo-holder (Gatan, Model 914.6) and cooled to ~100 K using liquid nitrogen. The specimen of COF-320-V-hydrated was prepared by dispersing COF-320-V into distilled water and dropped onto the copper grid with an ultrathin carbon membrane fixed by a self-locking tweezer. Upon removing the surrounding water, it was quickly cooled down in liquid nitrogen and transferred to TEM with a high-tilting cryo-holder (Gatan, Model 914.6). The details of crystallography data are shown in *SI Appendix*, section C.

Ex Situ Synchrotron PXRD Analyses. The synchrotron PXRD data were collected at the Beamline BL14B1 of Shanghai Synchrotron Radiation Facility (SSRF, $\lambda = 0.6887$ Å) equipped with the transmission mode capillary sample holder. The activated sample of COF-320-V was sealed in a glass capillary under a high vacuum after heating at 120 °C. The samples of COF-320-V loading different guest molecules were prepared by dosing desired vapor pressures into capillary holding with activated COF-320-V using the BELSORP MAXII system. The details of crystallography data are shown in *SI Appendix*, sections D and E.

In Situ PXRD Analyses during C_4H_{10} Adsorption. The in situ PXRD patterns were collected on a Bruker D8 advance diffractometer (Cu Kα, $\lambda = 1.5418$ Å) equipped with an Anton Parr hot-stage chamber with *n*-butane concentration controlled by mixing the dry N_2 with *n*-butane through a home-built system with two mass flow controllers (*SI Appendix*, Fig. S22). The PXRD patterns were collected repeatedly under a constant concentration until equilibrium and then switched to a different concentration for tracking the kinetics of structural transformation.

Theoretical Calculation. The RASPA software package (53) was used to conduct GCMC simulations to generate the adsorption isotherm. The frameworks are assumed to be rigid with fixed atoms in the grand canonical ensemble. The density-derived electrostatic and chemical method (54) was employed to calculate the net atom charges in the frameworks. CP2K software (55) was used for the DFT energy calculation to get the wave-function files and structure optimization using PBE12-D3(BJ) (56) exchange-correlation density functional with the DZVP-MOLOPT-SR-GTH basis set (57). Interaction analyses using the independent gradient model based on the Hirshfeld partition of molecular density (IGMH) method were conducted with Multiwfn software (42–43).

Data, Materials, and Software Availability. All study data are included in the article and/or supporting information.

ACKNOWLEDGMENTS. This work is supported by the National Natural Science Foundation of China (Nos. 22271189 and 22222108), the Science and Technology Commission of Shanghai Municipality (Nos. 21JC1401700, 21XD1402300, and 21DZ2260400), and the Double First-Class Initiative Fund of ShanghaiTech University (No. SYLDX0052022). High-resolution PXRD patterns were collected on the beamline BL14B at the SSRF. We thank the Berkeley Global Science Institute for the support of the scientific initiative, Prof. O. Terasaki for the support of EM facilities (#EM02161943) at ChEM of School of Physical Science and Technology (SPST), Dr. N. Yu, Dr. M. Peng, and Ms. L. Long for technical supports of XRD, NMR, and gas adsorption facilities at the Analytical Instrumentation Center (SPST-AIC10112914) at ShanghaiTech University, and the HPC Platform of ShanghaiTech University for theoretical calculation.

Author affiliations: [a]School of Physical Science and Technology, ShanghaiTech University, Shanghai 201210, China; [b]Shanghai Key Laboratory of High-Resolution Electron Microscopy, ShanghaiTech University, Shanghai 201210, China; [c]Shanghai Synchrotron Radiation Facility, Shanghai Advanced Research Institute, Chinese Academy of Sciences, Shanghai 201210, China; and [d]State Key Laboratory of Advanced Medical Materials and Devices, ShanghaiTech University, Shanghai 201210, China

1. O. M. Yaghi, M. J. Kalmutzki, C. S. Diercks, *Introduction to Reticular Chemistry: Metal-Organic Frameworks and Covalent Organic Frameworks* (Wiley-VCH, Weinheim, 2019), pp. 1–509.
2. S.-Y. Ding, W. Wang, Covalent organic frameworks (COFs): From design to applications. *Chem. Soc. Rev.* **42**, 548–568 (2013).
3. K. Geng *et al.*, Covalent organic frameworks: Design, synthesis, and functions. *Chem. Rev.* **120**, 8814–8933 (2020).
4. X. Guan, F. Chen, Q. Fang, S.-L. Qiu, Design and applications of three-dimensional covalent organic frameworks. *Chem. Soc. Rev.* **49**, 1357–1384 (2020).
5. B. Gui *et al.*, Three-dimensional covalent organic frameworks: From topology design to applications. *Acc. Chem. Res.* **53**, 2225–2234 (2020).
6. H. M. El-Kaderi *et al.*, Designed synthesis of 3D covalent organic frameworks. *Science* **316**, 268–272 (2007).
7. T. Ma *et al.*, Single-crystal X-ray diffraction structures of covalent organic frameworks. *Science* **361**, 48–52 (2018).
8. C. Gropp, T. Ma, N. Hanikel, O. M. Yaghi, Design of higher valency in covalent organic frameworks. *Science* **370**, 424 (2020).
9. S. Horike, S. Shimomura, S. Kitagawa, Soft porous crystals. *Nat. Chem.* **1**, 695–704 (2009).
10. S. Krause, N. Hosono, S. Kitagawa, Chemistry of soft porous crystals: Structural dynamics and gas adsorption properties. *Angew. Chem. Int. Ed. Engl.* **59**, 15325–15341 (2020).
11. J. D. Evans, V. Bon, I. Senkovska, H.-C. Lee, S. Kaskel, Four-dimensional metal-organic frameworks. *Nat. Commun.* **11**, 2690 (2020).
12. C. Gu *et al.*, Design and control of gas diffusion process in a nanoporous soft crystal. *Science* **363**, 387–391 (2019).
13. Y. Su *et al.*, Separating water isotopologues using diffusion-regulatory porous materials. *Nature* **611**, 289–294 (2022).
14. Y. Su *et al.*, Multi-component synthesis of a buta-1,3-diene-linked covalent organic framework. *J. Am. Chem. Soc.* **144**, 18218–18222 (2022).
15. Y. Su *et al.*, Hypercrosslinked polymer gels as a synthetic hybridization platform for designing versatile molecular separators. *J. Am. Chem. Soc.* **144**, 6861–6870 (2022).
16. S. Wang *et al.*, Efficient photocatalytic production of hydrogen peroxide using dispersible and photoactive porous polymers. *Nat. Commun.* **14**, 6891 (2023).
17. F. J. Uribe-Romo *et al.*, A crystalline imine-linked 3-D porous covalent organic framework. *J. Am. Chem. Soc.* **131**, 4570–4571 (2019).
18. Y.-B. Zhang *et al.*, Single-crystal structure of a covalent organic framework. *J. Am. Chem. Soc.* **135**, 16336–16339 (2013).
19. Y. Ma *et al.*, A dynamic three-dimensional covalent organic framework. *J. Am. Chem. Soc.* **139**, 4995–4998 (2017).
20. X. Han, J. Huang, C. Yuan, Y. Liu, Y. Cui, Chiral 3D covalent organic frameworks for high performance liquid chromatographic enantioseparation. *J. Am. Chem. Soc.* **140**, 892–895 (2018).
21. X. Guan *et al.*, Fast, ambient temperature and pressure ionothermal synthesis of three-dimensional covalent organic frameworks. *J. Am. Chem. Soc.* **13**, 4494–4498 (2018).
22. Y. Chen *et al.*, Guest-dependent dynamics in a 3D covalent organic framework. *J. Am. Chem. Soc.* **141**, 3298–3303 (2019).
23. T. Ma *et al.*, Diverse crystal size effects in covalent organic frameworks. *Nat. Commun.* **11**, 6128 (2020).
24. Z. Zhou *et al.*, Growth of single-crystal imine-linked covalent organic frameworks using amphiphilic amino-acid derivatives in water. *Nat. Chem.* **15**, 841–847 (2023).
25. B. Yu *et al.*, Linkage conversions in single-crystalline covalent organic frameworks. *Nat. Chem.*, 10.1038/s41557-023-01334-7 (2023).
26. T. Sun, L. Wei, Y. Chen, Y.-H. Ma, Y.-B. Zhang, Atomic-level characterization of dynamics of a 3D covalent organic framework by cryo-electron diffraction tomography. *J. Am. Chem. Soc.* **141**, 10962–10966 (2019).
27. T. Sun *et al.*, Direct-space structure determination of covalent organic frameworks from 3D electron diffraction data. *Angew. Chem. Int. Ed. Engl.* **59**, 22638–22644 (2020).
28. T. Sun, L. Wei, Y. Ma, Y.-B. Zhang, Unravelling crystal structures of covalent organic frameworks by electron diffraction tomography. *Chin. J. Chem.* **38**, 1153–1166 (2020).
29. Y. Ling *et al.*, Atomic-level structural responsiveness to environmental conditions from 3D electron diffraction. *Nat. Commun.* **13**, 6625 (2022).
30. W. Sun, P. Chen, M. Zhang, J.-X. Ma, J. Sun, Locating hydrogen positions for COF-300 by cryo-3D electron diffraction. *Angew. Chem. Int. Ed. Engl.* **62**, e202305985 (2023).
31. Y. Liu *et al.*, Topological isomerism in three-dimensional covalent organic frameworks. *J. Am. Chem. Soc.* **145**, 9679–9685 (2023).
32. L. Wei *et al.*, Guest-adaptive molecular sensing in a dynamic 3D co-valent organic framework. *Nat. Commun.* **13**, 7936 (2022).
33. Y. Xu *et al.*, Symmetry-breaking dynamics in a tautomeric 3D covalent organic framework. *Nat. Commun.* **14**, 4215 (2023).
34. X. Jiang *et al.*, Topochemical synthesis of single-crystalline hydrogen-bonded cross-linked organic frameworks and their guest-induced elastic expansion. *J. Am. Chem. Soc.* **141**, 10915–10923 (2019).
35. Q. Zhu *et al.*, 3D cage COFs: A dynamic three-dimensional covalent organic framework with high-connectivity organic cage nodes. *J. Am. Chem. Soc.* **142**, 16842–16848 (2020).

36. X. Liu *et al.*, A crystalline three-dimensional covalent organic framework with flexible building blocks. *J. Am. Chem. Soc.* **143**, 2123–2129 (2021).
37. J. Fang *et al.*, Piezochromism in dynamic three-dimensional covalent organic frameworks. *Angew. Chem. Int. Ed. Engl.* **62**, e202304234 (2023).
38. J. Li, J. Sui, L.-S. Cui, H.-L. Jiang, Hydrogen bonding regulated flexibility and disorder in hydrazone-linked covalent organic frameworks. *J. Am. Chem. Soc.* **145**, 1359–1366 (2023).
39. C. Kang *et al.*, Covalent organic framework atropisomers with multiple gas-triggered structural flexibilities. *Nat. Mater.* **22**, 636–643 (2023).
40. G. P. Moss, Basic terminology of stereochemistry (IUPAC Recommendations 1996). *Pure Appl. Chem.* **68**, 2193–2222 (1996).
41. A. L. Spek, Structure validation in chemical crystallography. *Acta Crystallogr. D Biol. Crystallogr.* **65**, 148–155 (2009).
42. T. Lu, F. Chen, Multiwfn: A multifunctional wavefunction analyzer. *J. Comput. Chem.* **33**, 580–592 (2012).
43. T. Lu, Q. Chen, Independent gradient model based on Hirshfeld partition: A new method for visual study of interactions in chemical systems. *J. Comput. Chem.* **43**, 539–555 (2022).
44. Y. He, W. Zhou, G. Qian, B. Chen, Methane storage in metal-organic frameworks. *Chem. Soc. Rev.* **43**, 5657–5678 (2014).
45. L. Zhu, Y.-B. Zhang, Crystallization of covalent organic frameworks for gas storage applications. *Molecules* **22**, 1149 (2017).
46. H. Furukawa, O. M. Yaghi, Storage of hydrogen, methane, and carbon dioxide in highly porous covalent organic frameworks for clean energy applications. *J. Am. Chem. Soc.* **131**, 8875–8883 (2009).
47. J. A. Mason *et al.*, Methane storage in flexible metal-organic frameworks with intrinsic thermal management. *Nature* **527**, 357–361 (2015).
48. M. O. Cichocka, J. Ångström, B. Wang, X. Zou, S. Smeets, High-throughput continuous rotation electron diffraction data acquisition via software automation. *J. Appl. Crystallogr.* **51**, 1652–1661 (2018).
49. W. Kabsch, XDS. *Acta Crystallogr. D Biol. Crystallogr.* **66**, 125–132 (2010).
50. G. M. Sheldrick, SHELXT–Integrated space-group and crystal-structure determination. *Acta Cryst. A Found. Adv.* **71**, 3–8 (2015).
51. G. M. Sheldrick, Crystal structure refinement with SHELXL. *Acta Crystallogr. C Struct. Chem.* **71**, 3–8 (2015).
52. O. V. Dolomanov, L. J. Bourhis, R. J. Gildea, J. A. K. Howard, H. Puschmann, OLEX2: A complete structure solution, refinement and analysis program. *J. Appl. Cryst.* **42**, 339–341 (2009).
53. D. Dubbeldam, S. Calero, D. E. Ellis, R. Q. Snurr, RASPA: Molecular simulation software for adsorption and diffusion in flexible nanoporous materials. *Mol. Simulat.* **42**, 81–101 (2016).
54. T. A. Manz, N. G. Limas, Introducing DDEC6 atomic population analysis: Part 1. Charge partitioning theory and methodology. *RSC Adv.* **6**, 47771–47801 (2016).
55. T. D. Kühne *et al.*, CP2K: An electronic structure and molecular dynamics software package-quickstep: Efficient and accurate electronic structure calculations. *J. Chem. Phys.* **152**, 194103 (2020).
56. S. Grimme, S. Ehrlich, L. Goerigk, Effect of the damping function in dispersion corrected density functional theory. *J. Comput. Chem.* **32**, 1456–1465 (2011).
57. J. VandeVondele, J. Hutter, Gaussian basis sets for accurate calculations on molecular systems in gas and condensed phases. *J. Chem. Phys.* **11**, 114105 (2007).